Second revision submitted to *Phys. Rev. Appl.* on 11/15/2024

Non-Local Spin Valve Optimization *via* Wide-Range Interfacial Resistance Tuning: Toward Spin Accumulation Sensors

Ben Kaiser, Justin Ramberger, Mikaela Norum, Nileena Nandakumaran, John Dewey, and Chris Leighton (leighton@umn.edu)

Department of Chemical Engineering and Materials Science, University of Minnesota, Minneapolis, Minnesota 55455, USA

Due to continued dimensional scaling, read sensors in hard disk drives face pressing challenges related to rising electrical resistance and thus impedance mismatch problems. All-metal, or at least low-resistance, magnetic field sensors are thus of high interest to displace current magnetic tunnel junction heads. Spin accumulation sensors based on metallic non-local spin valves (NLSVs) are promising candidates but need further signal optimization, particularly in the ultrathin limit required for applications. Here, we report a wide-ranging study of spin signal optimization in thin Al/AlO_x/Co-Fe-based NLSVs, using interfacial resistance-area-product tuning to mitigate spin back-diffusion. The Al-oxidation-controlled resistance-area product is tuned over 8 orders of magnitude, providing a complete picture of the evolution of the interfacial transport mechanism, spin signal, and non-local background. Signal improvements up to factors of almost 10^3 are obtained over transparent-interface devices (to ~0.15 Ω, or ~2 mΩμm^2), and the upper limit of feasible resistance-area product in NLSVs is established. Most significantly, the spin signals in such NLSVs at application-relevant resistances still lie substantially beneath theoretical limits, due to diminished tunneling spin polarization of unknown origin. Connecting tunneling devices to the transparent limit, a universal spin polarization *vs*. interfacial resistance-area product relation is thus uncovered in AlO_x-based devices, highlighting the specific issue limiting technological progress in this area. Potential strategies to achieve further gains are discussed in detail.

I. INTRODUCTION

Hard disk drive (HDD) technology continues to advance, largely driven by exponentially rising demand for cloud data storage [1]. HDDs have in fact reached storage densities over 1 Tb/in^2, fueled by technological advancements such as heat-assisted magnetic recording (HAMR) [2,3]. There exist multiple avenues to yet further improvements in HDDs, including through higher performance read head devices [4–7]. HDD readers currently employ ferromagnet/insulator/ferromagnet (F/I/F) magnetic tunnel junctions (MTJs), previously utilizing amorphous AlO_x-based tunnel barriers [8,9], now crystalline MgO_x-based tunnel barriers [10,11]. These MTJ reader sensors exhibit tunneling magnetoresistance (TMR) signals of 100s of %, even at room temperature [10–12], but now face a looming challenge. Specifically, this is an intrinsically resistive field sensing technology, with high resistance-area product (*RA*). At a given *RA*, as *A* is reduced in response to continual dimensional scaling, *R* increases, generating problematic issues with impedance matching, which is a critical issue at high data rates [4–7]. Optimal *R* values for impedance matching have in fact been surpassed in MTJ readers, creating challenges with signal-to-noise ratio (SNR), bit error rate (BER), *etc*. [4–7]. The response thus far has been to tune MgO_x tunnel barrier properties to reduce *RA*, but this comes at the cost of decreases in TMR and thus signal [6].

The ultimate solution to this problem is to switch to an alternative, all-metal, or at least low-*RA*, field sensing technology [4–7]. Substantial research is thus going into next-generation reader concepts such as current-perpendicular-to-plane (CPP) giant magnetoresistance (GMR) devices with highly-spin-polarized Fs [6,13–18], CPP GMR devices based on novel nonmagnetic (N) materials [19,20], and new concepts such as anomalous Hall effect sensors [21]. A particularly promising alternative to MTJs for future HDD readers, however, is the spin accumulation sensor

(SAS) [4–7], based on the metallic non-local spin valve (NLSV) [22–49]. NLSVs are now widely used in fundamental spintronics, as their unique geometry facilitates separation of charge and spin currents, enabling direct study of spin injection, transport, and relaxation [22–49]. As shown in Fig. 1(a), in a metallic NLSV, a charge current is injected from an F nanowire (the "injector") into an N nanowire (the "channel"), generating a non-equilibrium spin polarization in the N [22–50]. This results in a pure diffusive spin current in the N channel between the two Fs, leading to spin polarization at a second F (the "detector") at F-F separation d. This spin polarization at the second F is then detected through a non-local voltage (V_{NL}) or resistance (R_{NL}). Specifically, when the magnetizations of the two Fs are toggled between parallel (P) and antiparallel (AP) *via* application of an in-plane magnetic field (H), the change in the non-local resistance (ΔR_{NL}), or the NLSV "spin signal", is a direct measure of the spin polarization at the second N/F interface [22–50]. Through measurements of ΔR_{NL} *vs*. d, metallic NLSVs thus provide direct access to vital spin transport parameters such as the spin polarization of the diffusive current (α), the N spin diffusion length (λ_N), *etc*., making the NLSV an essential tool in metallic spintronics [22–49] and beyond [51–55].

Most importantly in the current context, as shown in Fig. 1(b), modifying the NLSV geometry leads to the SAS concept [4–7]. In essence, in this device, a single free F layer (F1) at the HDD air bearing surface (ABS) is coupled to a pinned F layer (F2) removed from the ABS, through a non-local spin current in a vertical N channel [4–7]. As the free F magnetization responds to the stray field from disk bits, ΔV_{NL} and ΔR_{NL} are modulated, providing the essential reader function. Several advantages of such SASs have been enumerated and explored, including intrinsically low RA, the low footprint at the ABS (where only one F and one N layer are needed), the favorable scaling with decreasing dimensions (the signal increases exponentially with decreasing d and geometrically with decreasing lateral dimensions), and favorable predicted SNR at high recording

densities [4–7]. The small ABS footprint is a particular advantage over current MTJ-based designs, potentially enabling substantial reductions in sensor stack thickness and shield-to-shield spacing, thereby improving SNR at high density.

There are of course also challenges with NLSV-based SASs. In all-metal transparent-interface F/N/F NLSVs, the spin signal ΔR_{NL} is in fact low, usually below 1 mΩ at typical device dimensions (*i.e.*, ~100 nm linewidths and d values of several hundred nm) [23–49], which is impractical for SASs. One of the primary causes of this low ΔR_{NL} is that spins injected from the F into the N metal channel are subject to efficient spin sinking back into the injector F due to its low spin resistance, greatly diminishing the non-equilibrium spin polarization in the N [50,56–58]. Quantitatively, the N spin resistance R_N and F spin resistance R_F are defined as $R_N = \frac{\rho_N \lambda_N}{A_N}$ and $R_F = \frac{\rho_F \lambda_F}{A}$, where $\rho_{N/F}$ is the N/F resistivity, $\lambda_{N/F}$ is the N/F spin diffusion length, A_N is the cross-sectional area of the N channel, and A is the F/N interface area. Because $\lambda_F << \lambda_N$, $R_F << R_N$, leading to the efficient spin back sinking. There is, however, a solution to this problem, which is to insert a moderate-RA barrier at the F/N interface to increase the spin resistance, thereby mitigating back diffusion [50,56–58]. For technologically competitive SASs, this mitigation of back diffusion would need to be effective at RA values low enough to still enable impedance matching at high recording densities, expected to be <1 Ωμm^2 [4–7]. In general terms, the effectiveness of finite-RA barriers at F/N interfaces in NLSVs is clear, as substantial boosts in ΔR_{NL} have been obtained with both AlO_x [24,25,27,28,35] and MgO_x [32,33] barriers. Amorphous AlO_x barriers are easily formed on Al, an N metal in which spin transport is efficient [24,25,27,28,35,47,48], making Al/AlO_x/F-based NLSVs attractive. In such devices, spin signals up to ~90 mΩ are frequently reported [24,28], increasing to 150-250 mΩ in some cases [27,35], and even ~1 Ω in rare

reports [25], the latter at *RA* products of 400-700 Ωμm^2 [25]. In NLSVs with MgO_x barriers, spin signals in excess of 100 mΩ have also been reported, but at lower *RA* (below 1 Ωμm^2 [32,33]), which is advantageous for SAS applications.

While these ΔR_{NL} enhancements *via* inclusion of intermediate-*RA* barriers in metallic NLSVs are promising, there are also clear limitations to our understanding of NLSV spin signal enhancement *via* increased *RA*. Most work has been performed at a single *RA* value, or over a narrow *RA* range, for example Refs. 24,27,35, with few studies systematically varying *RA* over a wide range [28,32]. Most of this work exploring finite-*RA* interfacial F/N barriers in metallic NLSVs has also been performed on devices with high N layer thickness t_N [24,28,32,35]. This is favorable for fundamental studies due to maximization of conductivity, mean-free-path, λ_N, ΔR_{NL}, *etc*., but untenable technologically. SASs in fact require t_N (which largely sets the shield-to-shield spacing (D_{ss}) in Fig. 1(b)) to be ~13.5 nm for recording at 5 Tb/in^2, for example [4]. This ultrathin-N-metal regime is poorly explored in NLSVs, and challenging to work in due to degradation of charge and spin transport properties, but essential for SASs [4]. Realistic SASs must also be based on technologically relevant F and N materials, ideally reasonably highly spin-polarized Fs, and N materials that do not exhibit the spin-transport Kondo effect [37–39,41,42,46]. The latter, present in Cu and Ag, but not Al [37], is highly deleterious to N spin transport due to efficient spin relaxation at magnetic impurities [37–39,41,42,46], including at room temperature [42].

Based on the above, what is urgently needed to fuel technological progress with SAS devices is a complete and systematic study of the quantitative impact of widely varied interfacial *RA* on the spin signal ΔR_{NL}, performed in a technologically relevant NLSV system, with ultrathin N layers of ~10 nm thickness. Such a study could answer numerous pressing questions, such as how high

ΔR_{NL} and $\Delta R_{NL}A$ can be driven by mitigation of spin back diffusion, the quantitative form of the ΔR_{NL} *vs*. *RA* relation, the resulting form of the temperature (*T*) dependence of ΔR_{NL}, particularly to 300 K, the interfacial transport mechanism as a function of *RA*, the maximum feasible *RA* at which NLSVs (and thus SASs) can be operated, and the device performance relative to theoretical predictions.

We address the above here through a detailed study of room-temperature-deposited $Al/AlO_x/Co_{78}Fe_{22}$-based NLSVs, where the Al and $Co_{78}Fe_{22}$ are technologically relevant N and F materials, the Al thickness is in the thin regime required for high-density recording using SASs (13 nm), and *RA* is tuned over ~8 orders of magnitude (10^{-3} Ωμm^2 < *RA* < 10^5 Ωμm^2) by controlling the oxidation of Al to AlO_x. Voltage- and *T*-dependent interfacial transport characterization reveals a crossover from diffusive to tunneling charge transport with increasing *RA*, which substantially boosts the NLSV spin signal. From the transparent limit to *RA* ≈ 500 Ωμm^2, ΔR_{NL} in fact increases by a factor of almost 10^3, reaching $\Delta R_{NL} \approx 0.15$ Ω or $\Delta R_{NL}A \approx 2$ mΩμm^2. The maximum feasible *RA* in such NLSVs (~1 kΩμm^2) is also understood from our data, corresponding to the point where ΔR_{NL} is overwhelmed by the non-local background resistance R_b. This upper limit on *RA* lies well above the region of interest for SASs, however, meaning that this should not limit this technology. Most importantly, despite the sizeable signal boosts, ΔR_{NL} at moderate *RA* remains substantially (1-2 orders of magnitude) beneath theoretical expectations based on analytical models. *Via* careful *d*-dependent analyses, we show that this underperformance derives from anomalously low tunneling spin polarization (*P*) at low *RA*. Connecting low-*RA* NLSV data with high-*RA* tunnel junction data, a universal *P*(*RA*) relation is thus uncovered (over almost 12 orders of magnitude in *RA*), highlighting the single factor currently limiting performance in such $N/AlO_x/F$-based NLSVs. On the basis of these findings, various routes to further performance gains are discussed.

II. METHODS

Si/Si-N/Al(13 nm)/AlO_x/$Co_{78}Fe_{22}$-based NLSVs were fabricated using varied Al oxidation conditions to tune the interfacial *RA*. Electron-beam lithography was first used to generate shadow masks from a PMMA/PMGI (PMMA = poly(methyl methacrylate), PMGI = poly (dimethylglutarimide)) bilayer resist (400 and 600 nm thickness, respectively) on Si/Si-N(300 nm) substrates (Fig. 2(a)), which generates a substantial resist undercut. The multi-angle deposition scheme in Fig. 2 (where the undercut is clear in panels (c-e)) was then used to fabricate all NLSVs in this work *via* electron-beam evaporation in an ultra-high vacuum (UHV) chamber with a base pressure of ~1×10^{-11} Torr. 15 nm of Al (from a 99.999% pure target) was first deposited at 5 Å s^{-1} (the high rate helping to minimize the Al surface roughness) at normal incidence to the substrate, as in Fig. 2(c,f). Transfer to the load lock of the UHV chamber was then performed, for room-temperature oxidation of the Al in O_2 (99.997%) at varied pressures (P_{O2} = 1×10^{-4} - 1.6×10^{2} Torr) for 20 min (Fig. 2(d,g)). As shown in the cross-sectional scanning transmission electron microscopy/energy dispersive X-ray spectroscopy (STEM/EDS) images in Supplemental Material Fig. S1 [59], this was found to typically result in a chemical AlO_x thickness of 3-5 nm and a remaining Al thickness of ~13 nm (as well as some oxidation at the Si-N interface [60]). The load lock was then pumped to UHV in ~2 min, and the devices returned to the growth chamber. Using an *in-situ* rotator, 32 nm of $Co_{78}Fe_{22}$ (from a 99.95% purity $Co_{80}Fe_{20}$ target [48]) was then deposited at 45° to the substrate, in the plane of the F electrodes, thereby shadowing the Al channel, as shown in Fig. 2(a,e,h). Our prior work reported extensive structural, chemical, and electrical characterization of such Co-Fe films [48]. Resist masks were then removed in NMP (N-methyl-2-pyrrolidone), yielding devices such as the one in the scanning electron microscopy (SEM) image

in Fig. 2(b). This process enables fabrication of Al/AlO_x/Co-Fe-based NLSVs with varied interfacial *RA*, with no break in vacuum. The nominal widths of the Al channel, left Co-Fe electrode, and right Co-Fe electrode, were 130, 180, and 110 nm, respectively, and at each oxidation condition, 60 devices were fabricated on each wafer, at multiple *d* (with high redundancy), for reliable determination of spin transport parameters.

Accurate physical dimensions of the NLSVs were measured from SEM images collected on JEOL JSM6010PLUS/LA, Hitachi SU8230, and Thermo Scientific Apreo 2S microscopes. Compositional characterization of the Co-Fe alloy films was done *via* energy-dispersive X-ray spectroscopy using the integrated EDS system in the JEOL JSM6010PLUS/LA. Temperature (*T*)-dependent (5 – 300 K) measurements of NLSVs were done in a Janis helium flow cryostat equipped with a 9-T superconducting magnet. Charge and spin transport measurements were made using a Lakeshore 370 AC resistance bridge with a 3708 preamplifying channel scanner, sourcing 316 μA at 13.7 Hz. At higher *RA* values, some interfacial resistance measurements were made with a Keithley 2400 source-measure unit.

III. RESULTS AND ANALYSIS

III.A INTERFACIAL TRANSPORT CHARACTERIZATION

Shown first in Fig. 3(a) is the measured (5-K) *RA* resulting from 20-min room-temperature Al oxidation at O_2 pressures up to 1.6×10^2 Torr, using the interfacial voltage (V_i) measurement configuration in Fig. 2(b). Note here that the data point at 10^{-10} Torr in Fig. 3(a) corresponds to no deliberate oxidation, *i.e.*, transparent F/N interfaces. *RA* is challenging to measure accurately and precisely in this limit, mainly due to NLSV non-idealities such as current spreading [37,49]. As discussed in detail in Supplemental Material Figs. S2, S3, S4, and their captions [59] (including

finite-element simulations [61]), our estimate for RA in this limit is ~1 × 10^{-3} Ωμm^2, as shown in the bottom left of Fig. 3(a). As P_{O2} is increased, RA first gradually increases, then rapidly in the ~10^{-5} to ~1 Torr range, before saturating near 10^5 Ωμm^2 (note the $\log_{10}$-$\log_{10}$ scale in Fig. 3(a)). These Al/AlO_x/$Co_{78}Fe_{22}$-based NLSVs thus span ~8 orders of magnitude in interfacial resistance (10^{-3} Ωμm^2 < RA < 10^5 Ωμm^2), a far larger range than in prior work. Note that for RA < 1 Ωμm^2 only, current spreading corrections have been applied to these data (throughout this paper), as described in Supplemental Material Figs. S2, S3, S4, and their captions [59]. In addition, there are two data sets shown in Fig. 3(a), where the solid points correspond to the main set of devices discussed throughout this paper and the open points are from a second device set. The overall level of reproducibility is good and the standard deviations on RA within a single set of devices on the same substrate were only ~30 % (across an 8 order of magnitude range).

As would be expected, the Al/Co-Fe interfacial conductance (G) *vs*. voltage (V) characteristics of the devices (again measured *via* the interfacial voltage (V_i) measurement configuration in Fig. 2(b)) vary greatly with the oxidation-controlled RA product. RA < 0.1 Ωμm^2 was found to result in $G(V)$ indistinguishable from ohmic, with only small voltages developed at feasible measurement currents (see Fig. S5 [59]), indicating negligible tunnel barriers. Higher RA values, however, result in the behavior shown in Fig. 3(b), which plots the 5-K conductance normalized to its $V = 0$ value, G/G_0. Already at RA = 0.4 Ωμm^2, relatively symmetric parabolic behavior is observed, suggestive of predominant tunneling transport [62–66]. As RA is increased further, this progressively evolves into a shallower and noticeably asymmetric and non-parabolic $G(V)$. Fig. 3(b) shows this only at relatively low V, whereas Fig. S5 [59] shows individual $G(V)$ curves over the full measurement range for each device. In the high-RA limit, such as the 500 Ωμm^2 - 40 kΩμm^2 devices shown in Figs. 3(b) and S5(d-f), the asymmetric non-parabolic form of $G(V)$ is reminiscent of that seen in

various compositions of AlO_x-based MTJs, where the asymmetry, including the hump feature at negative bias, has been ascribed to density-of-state effects in the F transition-metal electrodes [67,68].

Quantification of tunneling transport parameters was attempted through the usual Brinkman-Dynes-Rowell (BDR) approach, *i.e.*, a one-dimensional (1D) model of a trapezoidal tunnel barrier [64]. Fig. 3(b) shows the BDR fits only in the low-V limit (within ±0.1 V), whereas Fig. S5 shows the fits over a wider V range (up to 0.5 V), where poorer adherence to the BDR model is found, unsurprisingly given the aforementioned hump features due to transition-metal density-of-states effects [67,68]. Fig. 3(c) shows the P_{O2} dependence of the resulting low-V fit parameters, *i.e.*, $\bar{\varphi}$ the average tunnel barrier height and s the tunnel barrier thickness. (Further information is provided in Fig. S6 [59]). While it is well established that quantitative details from fitting to such simple models should be treated with substantial caution, several aspects of Fig. 3(c) are consistent with prior literature. The $\bar{\varphi}$ values are within the bounds of prior reports for AlO_x barriers [69–71], they increase with increasing P_{O2}, the typical inverse correlation between $\bar{\varphi}$ and s is clear [69–71], and the transport barrier thickness s [73] tends to 2-3 nm in the high-P_{O2} limit [69–71]. With the exception of the unusually large s at the lowest P_{O2}, which is likely related to the limited V range for the red data in Fig. 3(b), these fitting results are thus in reasonable agreement with prior work on AlO_x-based tunnel junctions [69–73]. The data in Figs. 3(b,c) are therefore consistent with diffusive, ohmic transport below ~0.1 $\Omega\mu m^2$, crossing over to tunneling transport at higher RA (corresponding to $P_{O2} > 10^{-3}$ Torr under our oxidation conditions).

The T dependence of the zero-bias resistance R further supports these conclusions. This is shown in Fig. 3(d), normalized to the low-T value, R(5 K), at various interfacial RA products. The

transparent-limit behavior here ($RA \approx 1 \times 10^{-3}$ Ωμm^2) displays a metallic form, *i.e.*, $dR/dT > 0$, with clear flattening below ~25 K. Increasing *RA* to just 0.03 Ωμm^2 weakens this metallic-like *T* dependence. All higher *RA* values then induce similar behavior, specifically the very weak insulating-like *R*(*T*) that is well-established as characteristic of tunneling transport [63,65,66]. We thus interpret the *R*(*T*) behavior in Fig. 3(d) as reflecting a crossover from clearly diffusive transport in the transparent interface case to tunneling transport at *RA* greater than approximately 0.1 Ωμm^2, consistent with the conclusions from *G*(*V*).

III.B NLSV PERFORMANCE AND ANALYSIS

Fig. 4(a) next addresses the critical issue of the effect of the interfacially tuned *RA* product on the non-local spin signal ΔR_{NL}. For illustrative purposes, this figure focuses on the low-*T* limit (5 K), at a fixed $d \approx 200$ nm. The spin signal in transparent interface devices is practically invisible on this scale, amounting to only 0.30 mΩ, consistent with our prior work on Al/$Co_{75}Fe_{25}$ NLSVs of comparable dimensions [48]. Increasing *RA* to just 0.03 Ωμm^2, however, increases the spin signal to 2.85 mΩ, *i.e.*, a signal enhancement of a factor of 9.5. This enhancement progressively continues from 0.4 Ωμm^2 through 500 Ωμm^2, reaching $\Delta R_{NL} = 0.14$ Ω by $RA = 500$ Ωμm^2, *i.e.*, a factor of ~500 enhanced over transparent interface Al/$Co_{78}Fe_{22}$ devices. Note that the variations in coercivity of the Co-Fe injector and detector apparent in Fig. 4(a) are irrelevant in the current context (clean switching and a well-defined AP state are achieved in all cases) but arise due to changes in the design of the F contact shape, along with some variability in the exact F width. Importantly, and as returned to and explained below, no data are shown in Fig. 4(a) above $RA \approx 1$ kΩμm^2, as devices in that regime were found to exhibit no measurable signals. Fig. 4(b) then shows the *T* dependence of ΔR_{NL} at the various *RA* values probed. The strong enhancements over

transparent-interface NLSVs are preserved across the entire T range, in particular to room temperature, where ΔR_{NL} = 57 mΩ is obtained at RA = 500 Ωμm^2, an enhancement over the transparent-interface case of a factor of 600. As discussed in Supplemental Material Fig. S7 [59], note that all data in Fig. 4 (and this entire paper) were taken at sufficiently low excitation current that ΔR_{NL} was independent of current, *i.e.*, the measurements are in the low-bias regime.

Deeper analysis of the contributions to the enhancement of ΔR_{NL} relative to transparent-interface NLSVs is provided in Fig. 5. Shown first in Fig. 5(a) is ΔR_{NL} *vs*. d at an illustrative temperature of 5 K, and various RA values. The overall enhancement of ΔR_{NL} with increasing RA is apparent, along with a clear evolution in the form of $\Delta R_{NL}(d)$. In the transparent limit, a relatively steep fall-off with d is seen, along with indications of an upturn from simple exponential behavior at low d (note that Fig. 5(a) is a $\log_{10}$-linear plot). As RA is increased, the exponential fall-off dampens, and simple exponential behavior prevails at all d, to as low as 100 nm in some cases. These findings are reinforced by fitting the data of Fig. 5(a) to the widely employed and validated Takahashi-Maekawa (TM) model [50]. This is a 1D model of NLSVs [50] based on the Valet-Fert model [74]. In its most general form, the TM model gives

$$\Delta R_{NL}^{general} = \frac{4\,R_N\left(\frac{P\,R_i}{(1-P^2)\,R_N}+\frac{\alpha\,R_F}{(1-\alpha^2)\,R_N}\right)^2 e^{-d/\lambda_N}}{\left(1+\frac{2\,R_i}{(1-P^2)\,R_N}+\frac{2\,R_F}{(1-\alpha^2)\,R_N}\right)^2 - e^{-2d/\lambda_N}} \qquad (1),$$

where $R_N = \frac{\rho_N \lambda_N}{A_N}$ and $R_F = \frac{\rho_F \lambda_F}{A}$ are the spin resistances of the N and F, R_i is the F/N interface resistance, and α and P are the diffusive- and tunneling-limit spin polarizations, respectively [50]. This general result for ΔR_{NL} is valid at all values of R_i, which essentially dictates (see Eqn. (1))

the relative importance of the diffusive and tunneling polarizations. Specifically in the transparent-interface limit, defined as $R_i << R_F$, Eqn. (1) becomes [50]

$$\Delta R_{NL}^{trans} = \frac{4\,R_N\left(\frac{\alpha\,R_F}{(1-\alpha^2)\,R_N}\right)^2 e^{-d/\lambda_N}}{\left(1+\frac{2\,R_F}{(1-\alpha^2)\,R_N}\right)^2 - e^{-2d/\lambda_N}} \qquad (2),$$

which is used in Fig. 5(a) only to fit the transparent-interface devices, with no Al oxidation, *i.e.*, the black points. This form approaches a pure exponential at high d, but with an upturn at low d (see the black curve in Fig. 5(a)) due to the aforementioned back-diffusion of injected spins from the N to the F due to the low R_F relative to R_N (because $\lambda_F << \lambda_N$). Conversely, in the tunneling limit, defined as $R_i >> R_{F/N}$, Eqn. (1) simplifies to [50]

$$\Delta R_{NL}^{tunnel} = R_N\,P^2 e^{-d/\lambda_N} \qquad (3),$$

i.e., a pure exponential decay controlled by λ_N, with a prefactor set only by R_N and P. The solid fit lines in Fig. 5(a) are to Eqn. (1) (except the black transparent-limit data), but thus represent an evolution from Eqn. (2) to Eqn. (3) with increasing RA.

The fits to the TM model in Fig. 5(a) were performed by applying the tightest parameter constraints possible [37,39,40,42,45,47,48]. All required NLSV dimensions were measured by SEM (nominal lithography values were not used) [37,39,40,42,45,47,48], $\rho_N(T)$ was measured *via* local transport measurements on the exact same NLSVs [37,39,40,42,45,47,48] (to avoid contact-resistance-related problems, transparent-interface results were used for the determination of $\rho_N(T)$), $\rho_F(T)$ was measured on $Co_{78}Fe_{22}$ nanowires with the same dimensions as our NLSVs [37,39,40,42,45,47,48], and $\lambda_F(T)$ was constrained using an approach we recently employed [48] based on known scaling with $\rho_F(T)$ [75,76]. Importantly, and as noted above, the

general TM model (Eqn. (1)) involves *two* interfacial spin polarizations: α, the spin polarization in the diffusive transport limit, and P, the spin polarization in the tunneling limit [50]. Fitting the transparent-interface data in Fig. 5(a) to Eqn. (2) yields α = 52% for these $Co_{78}Fe_{22}$ F layers, slightly decreased from the optimal 60% we recently reported for the $Co_{75}Fe_{25}$ composition [48]. (This shift in film composition occurred despite the use of the same nominally $Co_{80}Fe_{20}$ target, likely due to Co enrichment of the target over time). α was thus fixed at 52% to fit the remainder of the data in Fig. 5(a) to Eqn. (1). This leaves only P and λ_N as free parameters, which are readily separable, as, even in the transparent limit, λ_N alone controls the high-d (pure exponential) fall-off in Fig. 5(a) [50]. As is clear from the solid-line fits, the general TM model describes the data well at all RA, evolving from simple-exponential $\Delta R_{NL}(d)$ in the tunneling limit (high RA) to the characteristic low-d upturn in the transparent-interface limit (low RA) due to spin back diffusion.

Fig. 5(b,c) shows the T dependence of the parameters extracted from fits such as those shown in Fig. 5(a), *i.e.*, $\lambda_N(T)$ and $P(T)$ at various RA. The transparent-limit $\lambda_N(T)$ in Fig. 5(b) is unsurprising, revealing a weakly T-dependent λ_N near 150 nm, consistent with our prior work on Co/Al-based NLSVs at this t_N of 13 nm [47]. Unexpectedly, however, λ_N exhibits a clear increase with RA, saturating at ~450 nm at low T, *i.e.*, 3-fold enhanced relative to transparent-interface devices. This is not at all expected given that λ_N is a property of the entire Al channel, while RA is dictated by the Al/Co-Fe interface. Moreover, the surfaces of the Al channels in all of these devices are oxidized to AlO_x, the only difference being whether this occurs in air, after deposition (as for the transparent-interface devices), or controllably at some lower P_{O2} (as for the finite-RA devices). This suggests, intriguingly, that the precise manner in which the Al surface is oxidized has a significant impact on λ_N in the ultrathin limit, which will be discussed separately [77]. More

relevant to the current work is the behavior of P, which dominates ΔR_{NL} in the low-d limit. This is shown in Fig. 5(c), which also reveals a surprise. P is only weakly T dependent, as expected for $Co_{78}Fe_{22}$ [48], and increases with RA, but is strikingly small relative to accepted values from the tunneling literature. TMR measurements on F/AlO_x/F MTJs, and superconducting tunneling spectroscopy studies of F/AlO_x/S junctions, for example, typically yield P values of 40-60% for Co, Fe, and their alloys [78–80]. In comparison, in Fig. 5(c), P is below 5% at the lowest RA values probed, increasing only to a maximum of 10-15% at RA = 500 Ωμm^2. This immediately suggests that the spin signals in these Al/AlO_x/Co-Fe-based NLSVs are significantly limited by low tunneling spin polarization, which we now explore in detail.

Fig. 6(a) shows ΔR_{NL} *vs*. RA in the low-d (200 nm), low-T (5 K) limit (black points and line), highlighting the almost 10^3-fold increase in ΔR_{NL} from the transparent-interface limit to RA = 500 Ωμm^2. The transparent-limit (blue) and tunneling limit (gray) of the TM model are shaded on Fig. 6(a), based on $R_i << R_F$ and $R_i >> R_N$, respectively [50]. The solid red line then shows the prediction of the general TM model (Eqn. (1)), constraining all parameters to known values for our devices, fixing α = 52% (from the transparent-interface fit in Fig. 4(a)), and also putting P at 52%, for the purposes of comparison to the measured data. The red line saturates in the transparent and tunneling limits, as would be expected, increasing by a factor of ~10^4 between the two. Vitally, the measured ΔR_{NL} values lie substantially below the TM model prediction with 52% tunneling spin polarization for $Co_{78}Fe_{22}$, by factors of 60, 126, 62, and 20, at RA values of 0.03, 0.4, 14, and 500 Ωμm^2, respectively. Due to suppressed tunneling spin polarization, Al/AlO_x/$Co_{78}Fe_{22}$-based NLSVs thus exhibit substantially smaller spin signals than theoretically attainable, including in the intermediate RA region of highest relevance to SASs. As returned to below, this therefore

appears to be the dominant factor currently limiting the performance of AlO_x-based NLSVs for SAS applications. According to Fig. 6(a), at these device dimensions and other parameters, saturation of ΔR_{NL} at ~2.7 Ω could be achievable at $RA \approx 1$ Ωμm^2, compared to the largest experimental value in this work of $\Delta R_{NL} \approx 0.15$ Ω. We note that while the 1D nature of the TM model could limit its applicability to the 3D devices studied here, this concern should become irrelevant at higher *RA*, where the discrepancy between our data and the TM model remains. The underperformance of current devices relative to theoretical predictions is thus clear, as is its origin in terms of reduced tunneling polarization.

The comparison between experiment and theory in Fig. 6(a) also elucidates the origin of the upper limit of *RA* of ~1 kΩμm^2 for the experimental detection of a spin signal in these NLSVs (as in Fig. 4, for example). Fig. 6(b) explores this by plotting the experimental data on $\Delta R_{NL}(RA)$ along with the experimental data on $R_b(RA)$, *i.e.*, the NLSV background resistance, which was subtracted from the curves in Fig. 4(a). R_b starts well below 1 mΩ in the transparent-interface limit, consistent with many reports [37,44,45,49], then gradually increases with *RA* up to ~10-100 Ωμm^2, before rapidly increasing to $R_b \approx 1$ MΩ at $RA \approx 10^4$ Ωμm^2. R_b thus spans 10 orders of magnitude in the probed *RA* range, our $R_b(RA)$ being in reasonable agreement with scattered literature reports at low and moderate *RA* [24,27,28,35]. Critically, R_b increases more rapidly with *RA* than ΔR_{NL} does, the two curves in Fig. 6(b) crossing at ~25 Ωμm^2, indicating a background that exceeds the spin signal. The maximum theoretical ΔR_{NL} of ~2.7 Ω for our NLSVs (see Fig. 6(a)) is then crossed at ~300 Ωμm^2 (see the horizontal dashed line in Fig. 6(b)), very close to the maximum *RA* at which we found spin signals to be experimentally measurable (500 Ωμm^2). Quite simply, the effective upper

limit on the *RA* product of ~1 kΩμm^2 in these NLSVs is thus set by the rapidly increasing non-local background resistance, which swamps the spin signal at sufficiently high *RA*.

There are several important points to elaborate regarding this finding. First, the threshold we suggest here of ~1 kΩμm^2 is consistent with much literature data. To the best of our knowledge, the largest *RA* values at which working NLSVs have been reported are in the 440-700 Ωμm^2 range for AlO_x barriers [25], consistent with Fig. 6(b). Second, from the technological perspective, it is important to note that this upper range of ~1 kΩμm^2 will not limit the application of NLSVs as SASs, as the region of interest for *RA* for high-density recording in HDDs is expected to lie below ~1 Ωμm^2 [4–7], well below our measured limit. Third, the origin of R_b in NLSVs is understood to be a combination of current spreading and thermoelectric effects [30,31,34,36,44,49,81]. These phenomena have recently been quantitatively modeled in the transparent-interface limit for several F/N combinations in NLSVs [49], and this modelling could likely be extended to finite *RA*. Such understanding could open avenues to decrease R_b over the values shown in Fig. 6(b), thus increasing the maximum *RA* at which NLSV spin signals can be detected, and benefitting SAS development. Note also that in SAS devices in HDDs it is envisioned that relatively thick F metallic shields will flank the active device region (see Fig. 1(b)), which could provide substantial heat sinking, potentially mitigating some contributions to R_b.

With the origins of the effective upper limit of *RA* for metallic NLSVs and SASs understood, we now return to the key issue of the suppressed tunneling spin polarization, which largely limits the performance in Fig. 6(a). Taking the low-*T* limiting values of *P* from Fig. 5(c) and plotting them *vs*. *RA* results in Fig. 6(c) (red data points). Importantly, these *P* values are small, but remarkably consistent with the scattered prior reports on other AlO_x-barrier-based NLSVs, regardless of the F

employed. The data from our work using $Co_{78}Fe_{22}$ (red points), prior work using $Co_{50}Fe_{50}$ and $Ni_{80}Fe_{20}$ (orange points [25,35]), and prior work using Co (yellow points [24,27]), all lie on essentially the same curve, P increasing weakly with RA up to the ~1 kΩμm^2 limit, where it reaches ~15%. Yet more remarkably, this universal $P(RA)$ behavior in AlO_x-based NLSVs also connects with the $P(RA)$ behavior found in tunneling devices such as MTJs and F/I/S junctions. The blue and purple points in Fig. 6(c) are from literature on those types of devices [73,82], forming an apparently universal $P(RA)$ curve for AlO_x-based devices. Around the ~1 kΩμm^2 effective RA limit for NLSVs, P increases more rapidly with RA, before asymptotically approaching the roughly 45% value for Fe, Co (dashed and dotted horizontal lines in Fig. 6(c)), and most of their alloys [78–80]. Again, this entire behavior stands in contrast to the value of α in $Co_{78}Fe_{22}$, which lies at 52%. To our knowledge, this universal $P(RA)$ behavior, which extends over almost 12 orders of magnitude, has not been previously reported. Anomalously low P values in the relatively low-RA NLSV region have been reported previously, but with little comment [24,27,28,35], while the connection of the curves for NLSVs with $RA < 1$ kΩμm^2 with that for MTJs and F/I/S junctions with $RA > 1$ kΩμm^2, seems to have not been previously appreciated. The smooth connection of the NLSV $P(RA)$ data (red/orange/yellow points) with the tunneling device $P(RA)$ data (blue/purple points) is particularly noteworthy given the very different device geometries and heterostructures involved, a strong argument against an analysis artifact in a specific device type.

With respect to the origins of the behavior shown in Fig. 6(c), the $P(RA)$ relationship in AlO_x-based MTJs has been interpreted in terms of intrinsic variations in the contributions to tunneling from *s* and *d* electrons in transition-metal Fs [73]. Based on simple tunneling models, as RA is decreased, low-effective-mass *s* electrons from wide bands have been suggested to contribute to different extents to the tunnel current in amorphous (*i.e.*, non-spin-filtering) AlO_x-based tunnel junctions

relative to high-effective-mass *d* electrons from narrow bands [73]. The differing spin splitting and polarization of *d* and *s* electrons can then lead to varying *P* with reduced *RA*, which has been used to reproduce the *P vs*. AlO_x barrier thickness relationship in MTJs [73]. It is possible that this type of explanation could be relevant for the entire *P vs*. *RA* relation in Fig. 6(c), although it is unclear if features such as the change in slope around 10^3-10^4 Ωμm^2 could be reproduced in such models. Clearly, further theoretical work in this direction would be beneficial and could have a direct bearing on the development of NLSVs for SAS devices. While the cross-sectional areas of the F/N interfaces in these NLSVs are small (approximately 130 × 180 nm^2), other issues, such as pinholes [65,66], interfacial spin scattering, and parallel conduction mechanisms should also be considered. Regarding the latter, there appears to be generally insufficient understanding of spin-dependent transport across low-$\bar{\varphi}$, weak barriers, which play a vital role in low-*RA* devices of the type studied here. Numerous materials factors and defect issues could play a role in such barriers, although the behavior in Fig. 6(c) is strikingly independent of the device type, specific heterostructure, layer sequence, Al oxidation method, *etc*.

III.C OUTLOOK

While the data and analyses in Figs. 3-6 significantly elucidate the potential of intermediate-*RA* metallic NLSVs for SAS applications, several additional directions are worth exploring for further optimization. First and foremost, it may be possible to obtain further increases in ΔR_{NL} with essentially the same device architecture employed here. Consider Fig. 7, for example, which shows the data from this work and various other AlO_x-based NLSV literature reports, plotted as $\Delta R_{NL}A$ *vs*. *RA*, in the low-*T* limit. (As noted in the figure caption, these devices all have comparable *d*). Reasonably consistent behavior is found (the dashed fit line corresponds to a power law with

exponent ~0.42), and, notably, higher $\Delta R_{NL}A$ values were obtained in one case, Ref. [25] by Valenzuela and Tinkham. That study was performed on NLSVs with even lower t_N than in the current work, which, somewhat counterintuitively, could be the source of the improved spin signal. Looking at Eqn. (3), in the tunneling limit ($R_i >> R_{N/F}$) the materials parameters controlling the magnitude of ΔR_{NL} are λ_N, P, and $R_N = \rho_N\lambda_N/t_N w_N$, where w_N is the N width. As t_N is decreased (and thus ρ_N is increased), provided the increase in R_N is not outweighed by a decrease in λ_N, ΔR_{NL} can thus further increase. It is therefore of high interest to extend the current study to varied t_N, particularly to determine if an optimum t_N below 13 nm can be obtained at RA values relevant to SAS applications. Next, as already noted, improved understanding of the origin of R_b in these types of devices could lead to routes to decrease this background, which would be generally beneficial for applications, and could enable datasets such as those in Figs. 3-6 to be extended to higher RA (beyond 1 kΩμm^2) providing yet fuller understanding.

From Figs. 5(c), 6(a), and 6(c), however, it is clear that the primary barrier to further advancement in the optimization of NLSVs for SAS applications is suppressed tunneling spin polarization. Routes to circumvent this obviously hinge on a theoretical understanding of the universal $P(RA)$ in Fig. 6(c), but several experimental possibilities are apparent. There is a vast body of knowledge at this stage, for example, particularly in industry, regarding the engineering of tunnel barriers to impact specific aspects of MTJ performance [20,83–85], which could be brought to bear in metallic NLSVs with intermediate RA barriers. Repeating the type of study presented here in NLSVs with controlled-RA MgO_x-based barriers is of course also highly worthwhile. Fig. S8 [59] shows a plot of $\Delta R_{NL}A$ *vs*. RA, comparing our data on AlO_x-based NLSVs [25,27,35] with literature data on MgO_x-based NLSVs [32,33]. The latter devices employ thicker N layers [32,33], but nevertheless reveal a faster rise of the spin signal with RA, leading to comparable maximum ΔR_{NL},

but at $RA < 1\ \Omega\mu m^2$, of high interest for SAS applications. Extending such MgO_x-based NLSV studies to the low-t_N limit over the widest possible *RA* range would be of exceptional interest. It is also possible that different routes to low-*RA* barriers could be beneficial in NLSVs, such as the use of inherently lower energy barrier materials, such as Si, Ge, *etc*. Another interesting possibility that is obvious from Fig. 1(b), but seems to not yet have been fully explored, is asymmetric-interface NLSVs [43]. We refer here to devices with different interfacial *RA* products at each F/N interface [43]. Low *RA* in the charge-current-carrying leg in Fig. 1(b) combined with higher *RA* at the F/N interface near the ABS is particularly interesting in terms of potentially optimizing impedance matching while maximizing signal. Finally, it should be acknowledged that the data in Figs. 4-7 focus on the signal, ΔR_{NL}, not the SNR, which is the vital metric for read sensors. This study will thus hopefully also stimulate additional investigations of noise behavior in metallic NLSVs with varied *RA*.

IV. SUMMARY

This work provides a detailed and quantitative study of the transport mechanism, spin signal, background resistance, and extracted tunneling spin polarization as a function of Al-oxidation-controlled interfacial *RA* product in N/AlO_x/F-based NLSVs. Critically, this has been performed with technologically relevant N and F metals (Al and $Co_{78}Fe_{22}$, respectively), in the ultrathin-N limit relevant to application of SASs. A clear crossover from diffusive to tunneling transport is observed with increasing *RA*, accompanied by an enhancement of the spin signal by a factor approaching 10^3. Maximum spin signals of ~0.15 Ω are thus obtained, at ~500 $\Omega\mu m^2$ *RA* values. Nevertheless, quantitative comparisons of experimental data with simple theoretical predictions reveal a shortfall of 1-2 orders of magnitude at intermediate *RA*, which was found to predominantly

derive from suppressed tunneling spin polarization. Remarkably, such results on NLSVs connect smoothly with the *P vs*. *RA* behavior of tunneling devices such as MTJs and F/I/S junctions, uncovering a universal *P*(*RA*) relation in AlO_x-based devices, over almost 12 orders of magnitude in *RA*. These results thus pinpoint the single factor limiting the performance of current AlO_x-based NLSV for SAS applications; a number of potential routes to further gains have been discussed. We hope that this work will stimulate such future work, as well as theoretical studies aimed at explaining the universal *P*(*RA*) behavior.

ACKNOWLEDGMENTS: This work was primarily supported by Seagate Technology Inc., with additional support from the National Science Foundation through DMR-2103711 and the Advanced Storage Research Committee. Parts of this work were conducted in the Minnesota Nano Center, which is supported by NSF through the National Nanotechnology Coordinated Infrastructure under ECCS2025124, and in the UMN Characterization Facility, which is partially supported by NSF through the MRSEC program under DMR-2011401. We acknowledge M. Odlyzko and N. Seaton for assistance with STEM/EDX studies, and L. O'Brien, P. Crowell and O. Heinonen for useful comments and discussions.

REFERENCES

[1] B. Bhushan, Current status and outlook of magnetic data storage devices, Microsyst. Technol. **29**, 1529 (2023).

[2] M. H. Kryder, E. C. Gage, T. W. McDaniel, W. A. Challener, R. E. Rottmayer, G. Ju, Y.-T. Hsia, and M. F. Erden, Heat assisted magnetic recording, Proc. IEEE **96**, 1810 (2008).

[3] M. T. Kief and R. H. Victora, Materials for heat-assisted magnetic recording, MRS Bull. **43**, 87 (2018).

[4] M. Takagishi, K. Yamada, H. Iwasaki, H. N. Fuke, and S. Hashimoto, Magnetoresistance ratio and resistance area design of CPP-MR film for 2–5 Tb/in^2 read sensors, IEEE Trans. Magn. **46**, 2086 (2010).

[5] M. Yamada, D. Sato, N. Yoshida, M. Sato, K. Meguro, and S. Ogawa, Scalability of spin accumulation sensor, IEEE Trans. Magn. **49**, 713 (2013).

[6] T. Nakatani, Z. Gao, and K. Hono, Read sensor technology for ultrahigh density magnetic recording, MRS Bull. **43**, 106 (2018).

[7] G. Albuquerque, S. Hernandez, M. T. Kief, D. Mauri, and L. Wang, HDD reader technology roadmap to an areal density of 4 Tbpsi and beyond, IEEE Trans. Magn. **58**, 1 (2022).

[8] T. Miyazaki and N. Tezuka, Giant magnetic tunneling effect in Fe/Al_2O_3/Fe junction, J. Magn. Magn. Mater. **139**, L231 (1995).

[9] J. S. Moodera, L. R. Kinder, T. M. Wong, and R. Meservey, Large magnetoresistance at room temperature in ferromagnetic thin film tunnel junctions, Phys. Rev. Lett. **74**, 3273 (1995).

[10] S. Yuasa, T. Nagahama, A. Fukushima, Y. Suzuki, and K. Ando, Giant room-temperature magnetoresistance in single-crystal Fe/MgO/Fe magnetic tunnel junctions, Nat. Mater. **3**, 868 (2004).

[11] S. S. P. Parkin, C. Kaiser, A. Panchula, P. M. Rice, B. Hughes, M. Samant, and S.-H. Yang, Giant tunnelling magnetoresistance at room temperature with MgO (100) tunnel barriers, Nat. Mater. **3**, 862 (2004).

[12] T. Scheike, Z. Wen, H. Sukegawa, and S. Mitani, 631% room temperature tunnel magnetoresistance with large oscillation effect in CoFe/MgO/CoFe(001) junctions, Appl. Phys. Lett. **122**, 112404 (2023).

[13] S. Wurmehl, P. J. Jacobs, J. T. Kohlhepp, H. J. M. Swagten, B. Koopmans, S. Maat, M. J. Carey, and J. R. Childress, Local formation of a Heusler structure in CoFe–Al alloys, Appl. Phys. Lett. **98**, 012506 (2011).

[14] Y. K. Takahashi, S. Kasai, S. Hirayama, S. Mitani, and K. Hono, All-metallic lateral spin valves using $Co_2Fe(Ge_{0.5}Ga_{0.5})$ Heusler alloy with a large spin signal, Appl. Phys. Lett. **100**, 052405 (2012).

[15] K. Hamaya, N. Hashimoto, S. Oki, S. Yamada, M. Miyao, and T. Kimura, Estimation of the spin polarization for Heusler-compound thin films by means of nonlocal spin-valve measurements: Comparison of Co_2FeSi and Fe_3Si, Phys. Rev. B **85**, 100404 (2012).

[16] K. Kasahara, Y. Fujita, S. Yamada, K. Sawano, M. Miyao, and K. Hamaya, Greatly enhanced generation efficiency of pure spin currents in Ge using Heusler compound Co_2FeSi electrodes, Appl. Phys. Express **7**, 033002 (2014).

[17] S. Shirotori, S. Hashimoto, M. Takagishi, Y. Kamiguchi, and H. Iwasaki, All-metallic nonlocal spin valves using polycrystalline $Co_2(FeMn)Si$ Heusler alloy with large output, Appl. Phys. Express **8**, 023103 (2015).

[18] K. Elphick, W. Frost, M. Samiepour, T. Kubota, K. Takanashi, H. Sukegawa, S. Mitani, and A. Hirohata, Heusler alloys for spintronic devices: review on recent development and future perspectives, Sci. Technol. Adv. Mater. **22**, 235 (2021).
[19] K. Mukaiyama, S. Kasai, Y. K. Takahashi, K. Kondou, Y. Otani, S. Mitani, and K. Hono, High output voltage of magnetic tunnel junctions with a $Cu(In_{0.8}Ga_{0.2})Se_2$ semiconducting barrier with a low resistance–area product, Appl. Phys. Express **10**, 013008 (2017).
[20] T. Nakatani, S. Li, Y. Sakuraba, T. Furubayashi, and K. Hono, Advanced CPP-GMR Spin-valve sensors for narrow reader applications, IEEE Trans. Magn. **54**, 1 (2018).
[21] T. Nakatani, P. D. Kulkarni, H. Suto, K. Masuda, H. Iwasaki, and Y. Sakuraba, Perspective on nanoscale magnetic sensors using giant anomalous Hall effect in topological magnetic materials for read head application in magnetic recording, Appl. Phys. Lett. **124**, 070501 (2024).
[22] M. Johnson and R. H. Silsbee, Interfacial charge-spin coupling: injection and detection of spin magnetization in metals, Phys. Rev. Lett. **55**, 1790 (1985).
[23] F. J. Jedema, A. T. Filip, and B. J. Van Wees, Electrical spin injection and accumulation at room temperature in an all-metal mesoscopic spin valve, Nature **410**, 345 (2001).
[24] F. J. Jedema, H. B. Heersche, A. T. Filip, J. J. A. Baselmans, and B. J. van Wees, Electrical detection of spin precession in a metallic mesoscopic spin valve, Nature **416**, 713 (2002).
[25] S. O. Valenzuela and M. Tinkham, Spin-polarized tunneling in room-temperature mesoscopic spin valves, Appl. Phys. Lett. **85**, 5914 (2004).
[26] Y. Ji, A. Hoffmann, J. S. Jiang, and S. D. Bader, Spin injection, diffusion, and detection in lateral spin-valves, Appl. Phys. Lett. **85**, 6218 (2004).
[27] N. Poli, M. Urech, V. Korenivski, and D. B. Haviland, Spin-flip scattering at Al surfaces, J. Appl. Phys. **99**, 08H701 (2006).
[28] A. Vogel, J. Wulfhorst, and G. Meier, Enhanced spin injection and detection in spin valves with integrated tunnel barriers, Appl. Phys. Lett. **94**, 122510 (2009).
[29] F. Casanova, A. Sharoni, M. Erekhinsky, and I. K. Schuller, Control of spin injection by direct current in lateral spin valves, Phys. Rev. B **79**, 184415 (2009).
[30] F. L. Bakker, A. Slachter, J.-P. Adam, and B. J. van Wees, Interplay of peltier and seebeck effects in nanoscale nonlocal spin valves, Phys. Rev. Lett. **105**, 136601 (2010).
[31] A. Slachter, F. L. Bakker, J.-P. Adam, and B. J. Van Wees, Thermally driven spin injection from a ferromagnet into a non-magnetic metal, Nat. Phys. **6**, 879 (2010).
[32] Y. Fukuma, L. Wang, H. Idzuchi, S. Takahashi, S. Maekawa, and Y. Otani, Giant enhancement of spin accumulation and long-distance spin precession in metallic lateral spin valves, Nat. Mater. **10**, 527 (2011).
[33] L. Wang, Y. Fukuma, H. Idzuchi, G. Yu, Y. Jiang, and Y. Otani, Effect of annealing on interfacial spin polarization and resistance in permalloy/MgO/Ag lateral spin valves, Appl. Phys. Express **4**, 093004 (2011).
[34] S. Hu and T. Kimura, Anomalous Nernst-Ettingshausen effect in nonlocal spin valve measurement under high-bias current injection, Phys. Rev. B **87**, 014424 (2013).
[35] J.-C. Rojas Sánchez, P. Laczkowski, W. F. Savero Torres, M. Cubukcu, V. D. Nguyen, L. Notin, C. Beigné, C. Vergnaud, A. Marty, M. Jamet, L. Vila, and J. P. Attané, In-plane and out-of-plane spin precession in lateral spin-valves, Appl. Phys. Lett. **102**, 132408 (2013).
[36] S. Kasai, S. Hirayama, Y. K. Takahashi, S. Mitani, K. Hono, H. Adachi, J. Ieda, and S. Maekawa, Thermal engineering of non-local resistance in lateral spin valves, Appl. Phys. Lett. **104**, 162410 (2014).

[37] L. O'Brien, M. J. Erickson, D. Spivak, H. Ambaye, R. J. Goyette, V. Lauter, P. A. Crowell, and C. Leighton, Kondo physics in non-local metallic spin transport devices, Nat. Commun. **5**, 3927 (2014).
[38] J. T. Batley, M. C. Rosamond, M. Ali, E. H. Linfield, G. Burnell, and B. J. Hickey, Spin relaxation through Kondo scattering in Cu/Py lateral spin valves, Phys. Rev. B **92**, 220420 (2015).
[39] L. O'Brien, D. Spivak, J. S. Jeong, K. A. Mkhoyan, P. A. Crowell, and C. Leighton, Interdiffusion-controlled Kondo suppression of injection efficiency in metallic nonlocal spin valves, Phys. Rev. B **93**, 014413 (2016).
[40] L. O'Brien, D. Spivak, N. Krueger, T. A. Peterson, M. J. Erickson, B. Bolon, C. C. Geppert, C. Leighton, and P. A. Crowell, Observation and modelling of ferromagnetic contact-induced spin relaxation in Hanle spin precession measurements, Phys. Rev. B **94**, 094431 (2016).
[41] K.-W. Kim, L. O'Brien, P. A. Crowell, C. Leighton, and M. D. Stiles, Theory of Kondo suppression of spin polarization in nonlocal spin valves, Phys. Rev. B **95**, 104404 (2017).
[42] J. D. Watts, J. S. Jeong, L. O'Brien, K. A. Mkhoyan, P. A. Crowell, and C. Leighton, Room temperature spin Kondo effect and intermixing in Co/Cu non-local spin valves, Appl. Phys. Lett. **110**, 222407 (2017).
[43] L. Wang, W. Liu, H. Ying, L. Chen, Z. Lu, S. Han, S. Chen, B. Zhao, X. Xu, and Y. Jiang, Spin injection and detection in lateral spin valves with hybrid interfaces, Appl. Phys. Express **11**, 063004 (2018).
[44] R. K. Bennet, A. Hojem, and B. L. Zink, Thermal gradients and anomalous Nernst effects in membrane-supported nonlocal spin valves, Phys. Rev. B **100**, 104404 (2019).
[45] J. D. Watts, L. O'Brien, J. S. Jeong, K. A. Mkhoyan, P. A. Crowell, and C. Leighton, Magnetic impurities as the origin of the variability in spin relaxation rates in Cu-based spin transport devices, Phys. Rev. Mater. **3**, 124409 (2019).
[46] X. Shen and Y. Ji, Scaling of Kondo spin relaxation: Experiments on Cu-based nonlocal spin valves with Fe impurities, Phys. Rev. B **104**, 085101 (2021).
[47] J. D. Watts, J. T. Batley, N. A. Rabideau, J. P. Hoch, L. O'Brien, P. A. Crowell, and C. Leighton, Finite-size effect in phonon-induced Elliott-Yafet spin relaxation in Al, Phys. Rev. Lett. **128**, 207201 (2022).
[48] B. Kaiser, J. Ramberger, J. D. Watts, J. Dewey, and C. Leighton, High spin polarization and spin signal enhancement in non-local spin valves with Co–Fe alloy injectors and detectors, APL Mater. **11**, 051108 (2023).
[49] A.J. Wright, D. Bromley, J. Watts, J. Ramberger, B. Kaiser, M. J. Erickson, P. A. Crowell, C. Leighton, and L. O'Brien, Origins of background signal effects in all-metallic non-local spin valves, submitted, Phys. Rev. Mater (2024).
[50] S. Takahashi and S. Maekawa, Spin injection and detection in magnetic nanostructures, Phys. Rev. B **67**, 052409 (2003).
[51] A. T. Filip, B. H. Hoving, F. J. Jedema, B. J. van Wees, B. Dutta, and S. Borghs, Experimental search for the electrical spin injection in a semiconductor, Phys. Rev. B **62**, 9996 (2000).
[52] I. Appelbaum, B. Huang, and D. J. Monsma, Electronic measurement and control of spin transport in silicon, Nature **447**, 295 (2007).

[53] X. Lou, C. Adelmann, S. A. Crooker, E. S. Garlid, J. Zhang, K. S. M. Reddy, S. D. Flexner, C. J. Palmstrøm, and P. A. Crowell, Electrical detection of spin transport in lateral ferromagnet–semiconductor devices, Nat. Phys. **3**, 197 (2007).
[54] J. M. Kikkawa and D. D. Awschalom, Lateral drag of spin coherence in gallium arsenide, Nature **397**, 139 (1999).
[55] E. C. Ahn, 2D materials for spintronic devices, npj 2D Mater. Appl. **4**, 17 (2020).
[56] G. Schmidt, D. Ferrand, L. W. Molenkamp, A. T. Filip, and B. J. Van Wees, Fundamental obstacle for electrical spin injection from a ferromagnetic metal into a diffusive semiconductor, Phys. Rev. B **62**, R4790 (2000).
[57] E. I. Rashba, Theory of electrical spin injection: Tunnel contacts as a solution of the conductivity mismatch problem, Phys. Rev. B **62**, R16267 (2000).
[58] A. Fert and H. Jaffrès, Conditions for efficient spin injection from a ferromagnetic metal into a semiconductor, Phys. Rev. B **64**, 184420 (2001).
[59] See supplemental material at [URL] for additional data and information on: STEM/EDX characterization, current spreading simulations and estimations of transparent-interface *RA*, conductance-voltage data and fitting, dependence of the spin signal on injection current, and literature comparisons on spin signal *vs*. *RA*.
[60] V. M. Bermudez, Wet-chemical treatment of Si_3N_4 surfaces studied using infrared attenuated total reflection spectroscopy, J. Electrochem. Soc. **152**, F31 (2005).
[61] COMSOL Multiphysics® v. 6.2. www.comsol.com. COMSOL AB, Stockholm, Sweden.
[62] J. G. Simmons, Generalized formula for the electric tunnel effect between similar electrodes separated by a thin insulating film, J. Appl. Phys. **34**, 1793 (1963).
[63] E. Burstein and S. Lundqvist, editors, *Tunneling Phenomena in Solids* (Springer US, Boston, MA, 1969).
[64] W. F. Brinkman, R. C. Dynes, and J. M. Rowell, Tunneling conductance of asymmetrical barriers, J. Appl. Phys. **41**, 1915 (1970).
[65] B. J. Jönsson-Åkerman, R. Escudero, C. Leighton, S. Kim, I. K. Schuller, and D. A. Rabson, Reliability of normal-state current–voltage characteristics as an indicator of tunnel-junction barrier quality, Appl. Phys. Lett. **77**, 1870 (2000).
[66] D. A. Rabson, B. J. Jönsson-Åkerman, A. H. Romero, R. Escudero, C. Leighton, S. Kim, and I. K. Schuller, Pinholes may mimic tunneling, J. Appl. Phys. **89**, 2786 (2001).
[67] P. LeClair, J. T. Kohlhepp, C. H. Van De Vin, H. Wieldraaijer, H. J. M. Swagten, W. J. M. De Jonge, A. H. Davis, J. M. MacLaren, J. S. Moodera, and R. Jansen, Band structure and density of states effects in Co-based magnetic tunnel junctions, Phys. Rev. Lett. **88**, 107201 (2002).
[68] G. M. McKusky, Density of states effects in nickel based magnetic tunnel junctions, Ph.D. thesis, University of Minnesota, 2009.
[69] K. H. Gundlach and J. Hölzl, Logarithmic conductivity of Al-Al_2O_3-Al tunneling junctions produced by plasma- and by thermal oxidation, Surf. Sci. **27**, 125 (1971).
[70] J. Kadlec and K. H. Gundlach, Dependence of the barrier height on insulator thickness in Al-(Al-oxide)-Al sandwiches, Solid State Commun. **16**, 621 (1975).
[71] K. Gloos, P. J. Koppinen, and J. P. Pekola, Properties of native ultrathin aluminium oxide tunnel barriers, J. Phys. Condens. Matter **15**, 1733 (2003).
[72] N. Arakawa, Y. Otaka, and K. Shiiki, Evaluation of barrier height and thickness in tunneling junctions by numerical calculation on tunnel probability, Thin Solid Films **505**, 67 (2006).

[73] M. Münzenberg and J. S. Moodera, Superconductor-ferromagnet tunneling measurements indicate s p -spin and d -spin currents, Phys. Rev. B **70**, 060402 (2004).
[74] T. Valet and A. Fert, Theory of the perpendicular magnetoresistance in magnetic multilayers, Phys. Rev. B **48**, 7099 (1993).
[75] J. Bass and W. P. Pratt, Spin-diffusion lengths in metals and alloys, and spin-flipping at metal/metal interfaces: an experimentalist's critical review, J. Phys. Condens. Matter **19**, 183201 (2007).
[76] C. Ahn, K.-H. Shin, R. Loloee, J. Bass, and W. P. Pratt, Current-perpendicular-to-plane spin transport properties of CoFe alloys: Spin diffusion length and scattering asymmetry, J. Appl. Phys. **108**, 023908 (2010).
[77] B. Kaiser, J. Ramberger, M. Norum, N. Nandakumaran, J. Dewey, and C. Leighton, unpublished (2024).
[78] P. M. Tedrow and R. Meservey, Spin polarization of electrons tunneling from films of Fe, Co, Ni, and Gd, Phys. Rev. B **7**, 318 (1973).
[79] D. J. Monsma and S. S. P. Parkin, Spin polarization of tunneling current from ferromagnet/Al_2O_3 interfaces using copper-doped aluminum superconducting films, Appl. Phys. Lett. **77**, 720 (2000).
[80] S. V. Karthik, T. M. Nakatani, A. Rajanikanth, Y. K. Takahashi, and K. Hono, Spin polarization of Co–Fe alloys estimated by point contact Andreev reflection and tunneling magnetoresistance, J. Appl. Phys. **105**, 07C916 (2009).
[81] B. L. Zink, Thermal effects in spintronic materials and devices: An experimentalist's guide, J. Magn. Magn. Mater. **564**, 170120 (2022).
[82] S. Joo, K. Y. Jung, K. I. Jun, D. S. Kim, K. H. Shin, J. K. Hong, B. C. Lee, and K. Rhie, Spin-filtering effect of thin Al_2O_3 barrier on tunneling magnetoresistance, Appl. Phys. Lett. **104**, 152407 (2014).
[83] Y. Nagamine, H. Maehara, K. Tsunekawa, D. D. Djayaprawira, N. Watanabe, S. Yuasa, and K. Ando, Ultralow resistance-area product of $0.4\Omega(\mu m)^2$ and high magnetoresistance above 50% in CoFeB⁄MgO⁄CoFeB magnetic tunnel junctions, Appl. Phys. Lett. **89**, 162507 (2006).
[84] I. Ikhtiar, S. Kasai, P.-H. Cheng, T. Ohkubo, Y. K. Takahashi, T. Furubayashi, and K. Hono, Magnetic tunnel junctions with a rock-salt-type $Mg_{1-x}Ti_xO$ barrier for low resistance area product, Appl. Phys. Lett. **108**, 242416 (2016).
[85] S. Yuasa, K. Hono, G. Hu, and D. C. Worledge, Materials for spin-transfer-torque magnetoresistive random-access memory, MRS Bull. **43**, 352 (2018).

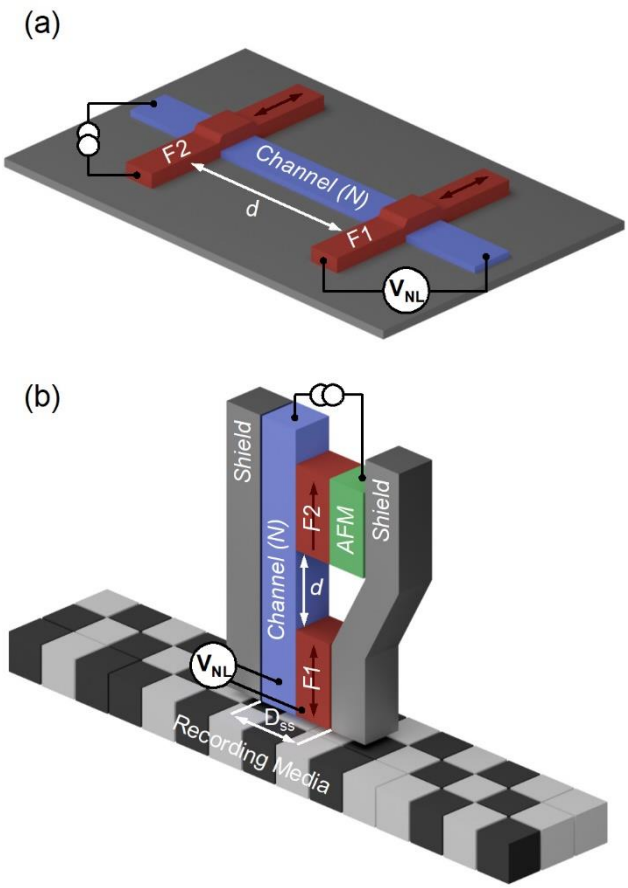

Fig. 1. (a) Schematic metallic NLSV highlighting the nonmagnetic metal (N) nanowire channel crossed by two ferromagnetic metals (F1, F2) at separation *d*. Also shown are the current and voltage arrangement for a non-local measurement. (b) Schematic spin accumulation sensor (SAS) hard-disk drive reader based on the NLSV geometry. F1 here is the free layer, F2 is the fixed layer, and also shown are an antiferromagnetic metallic (AFM) pinning layer (green), two shields (gray), the recording medium (bottom), and the schematic wiring arrangement. D_{ss} is the shield-to-shield spacing.

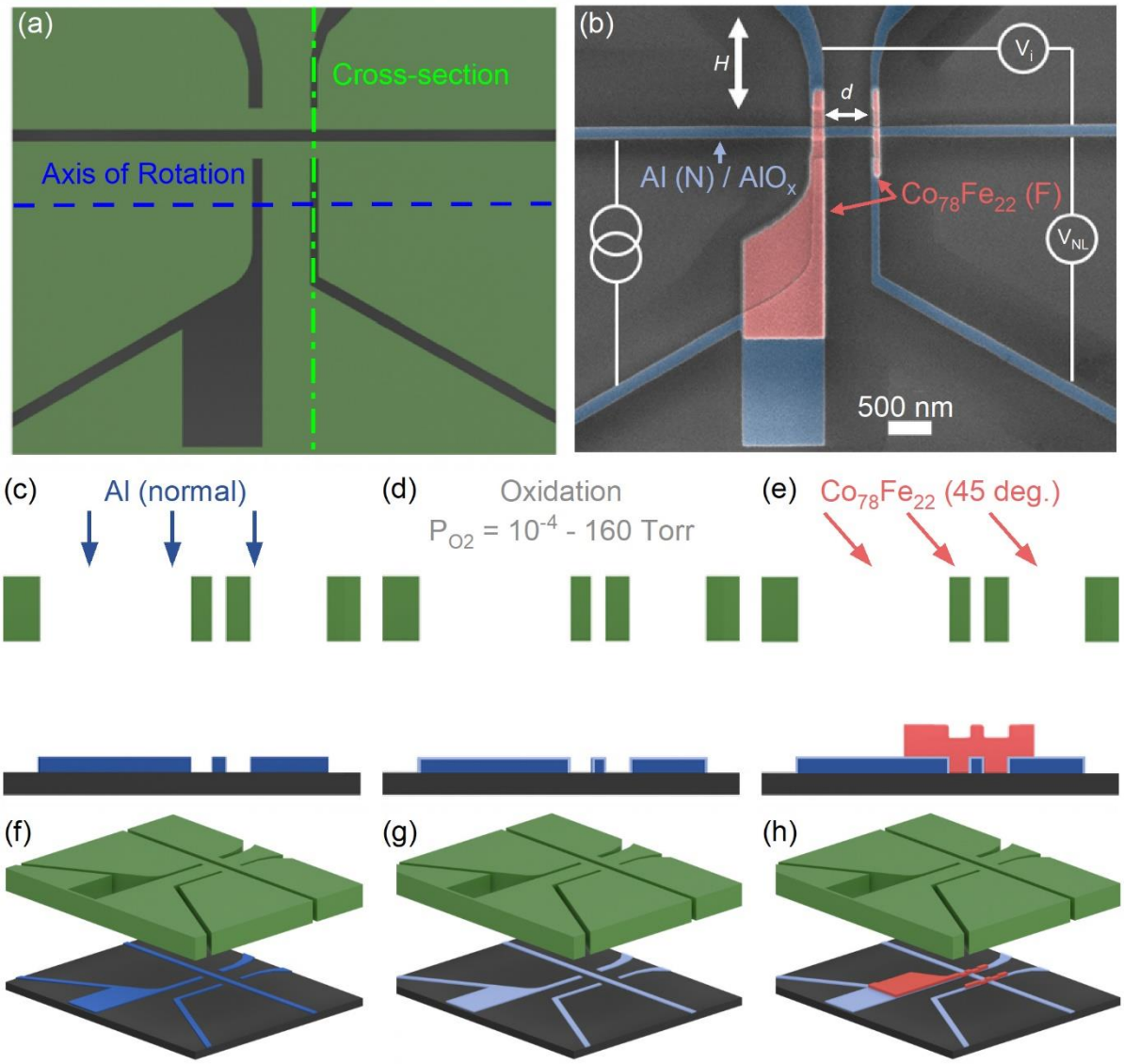

Fig. 2. (a) Top-view schematic of PMMA/PMGI shadow masks fabricated by electron-beam lithography, showing the axis of rotation for multi-angle deposition. (b) Scanning electron micrograph of a representative final NLSV, highlighting the nonmagnetic (N) Al channel, ferromagnetic (F) $Co_{78}Fe_{22}$ injector and detector, and the edge-to-edge F separation *d*. The left F electrode is wider, and has a nucleation pad, to promote differing coercivities in the two Fs, and thus clean switching (see Fig. 4(a)). Superimposed on Fig. 1(b) are wiring diagrams for the measurement of interface voltage (V_i, for measurement of the resistance-area product) and non-local voltage (V_{NL}); the in-plane applied magnetic field (H) is also shown. (c-e) Cross-sections (see (a)) of the shadow mask and Si/Si-N substrate after (c) deposition of Al normal to the mask, (d)

oxidation of the deposited Al in O_2 at pressures from 1×10^{-4} to 1.6×10^{2} Torr, and (e) $Co_{78}Fe_{22}$ deposition at 45° from the normal to the mask/substrate, projecting it to the right and completing the NLSV. Note the suspended mask appearance due to the substantial undercut in the PMMA/PMGI resist bilayer. (f-h) Orthographic views corresponding to (c-e).

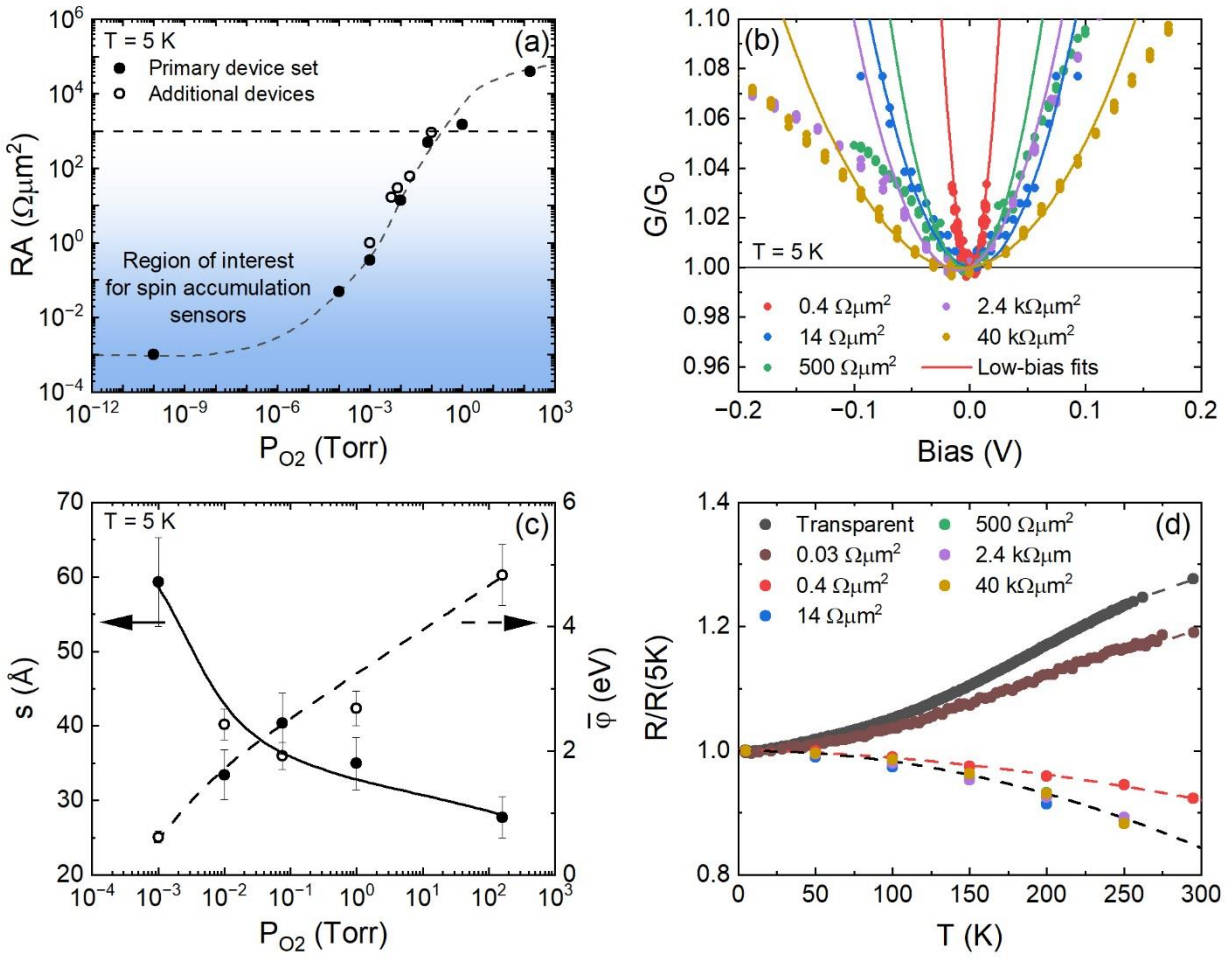

Fig. 3. (a) 5-K resistance-area product (*RA*) of Al/AlO_x/$Co_{78}Fe_{22}$-based NLSVs as a function of the O_2 pressure (P_{O2}) used in the 20-min room-temperature oxidation of Al to AlO_x. Data are shown for the primary set of devices studied in this work (solid points) as well as a second device set (open points). Note the $\log_{10}$-$\log_{10}$ scale. The region of interest for spin accumulation sensors is shaded blue, the horizontal dashed line marks the ~1 kΩμm^2 limit discussed in the text, and the dashed line through the points is a guide to the eye. (b) 5-K bias voltage dependence of the normalized conductance (G/G_0) at various *RA* values (points) along with low-*V* fits (lines) to the asymmetric tunnel barrier model described in the text [64]. Individual plots to higher *V* (where available) are shown in Fig. S5 [59]. (c) Tunnel barrier thickness (*s*, left axis) and average barrier height ($\bar{\varphi}$, right axis) extracted from the fits in (b), plotted *vs*. P_{O2}. Solid and dashed lines are guides to the eye and the error bars are standard errors from fits. (d) Temperature (*T*) dependence of the normalized zero-bias resistance ($R/R(5\text{ K})$) at various *RA* values. Dashed lines are guides to the eye.

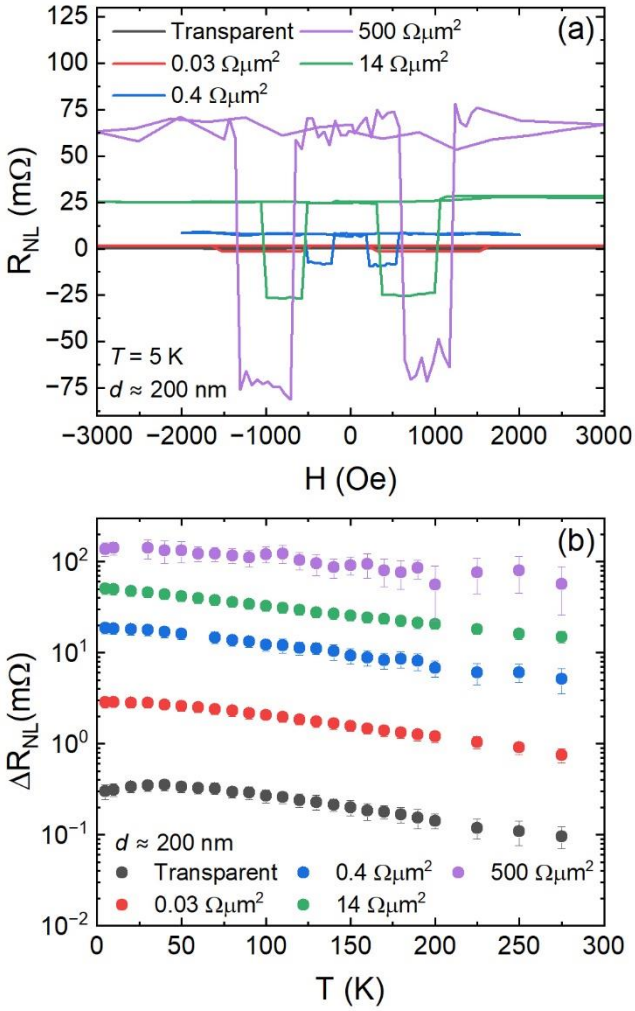

Fig. 4. (a) 5-K, background-subtracted non-local resistance (R_{NL}) *vs*. applied in-plane field (H) for representative Al/AlO_x/$Co_{78}Fe_{22}$-based NLSVs at various resistance-area product (RA) values. Each device has ferromagnet separation $d \approx 200$ nm. (b) Temperature (T) dependence of the non-local resistance change (ΔR_{NL}, note the $\log_{10}$ scale) at the same RA values and same $d \approx 200$ nm. Error bars are from the standard deviations in the parallel and antiparallel states and the total uncertainty on the measurement of device dimensions.

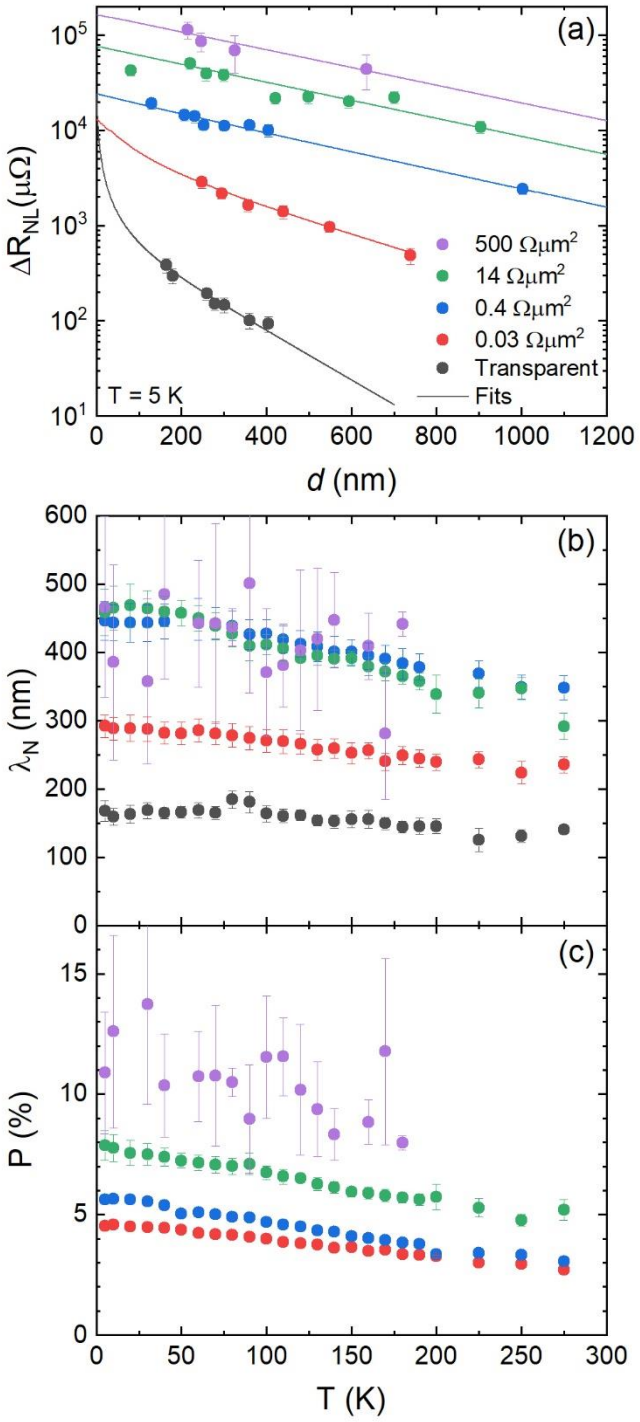

Fig. 5. (a) Ferromagnet separation (d) dependence of the 5-K non-local resistance change (ΔR_{NL}, note the $\log_{10}$ scale) of Al/AlO_x/$Co_{78}Fe_{22}$-based NLSVs at various resistance-area product (RA) values. The solid lines are fits to the general Takahashi-Maekawa model described in the text (Eqn. 1) [50]. Error bars are from the standard deviations in the parallel and antiparallel states and the

total measurement uncertainty of the device dimensions. (b,c) Temperature (T) dependence of (b) the extracted Al spin diffusion length (λ_N) and (c) the extracted tunneling spin polarization (P), again at various RA values. The error bars in (b) and (c) are standard errors from the fitting procedure.

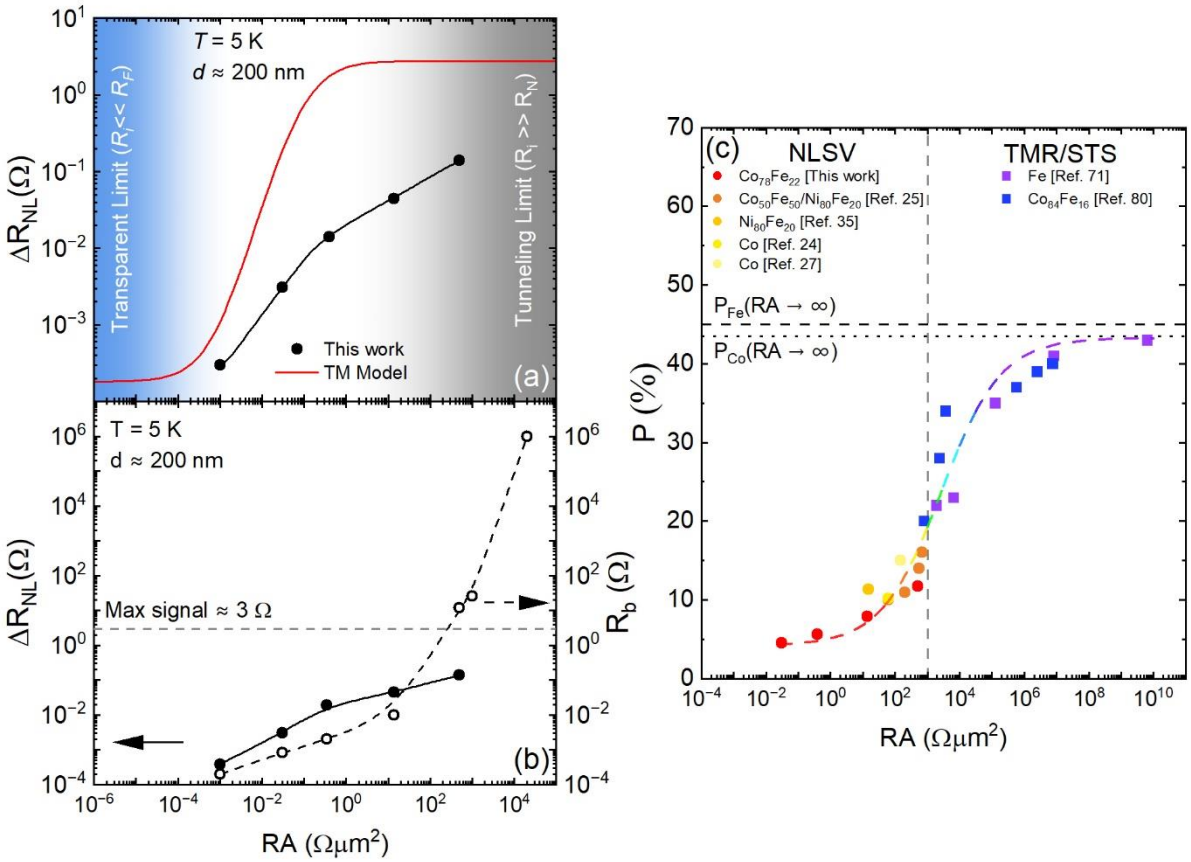

Fig. 6. (a) Resistance-area product (*RA*) dependence of the 5-K non-local resistance change (ΔR_{NL}) of Al/AlO$_x$/Co$_{78}$Fe$_{22}$-based NLSVs at ferromagnet-ferromagnet separation $d \approx 200$ nm. The black points are data, the black line is a guide to the eye, and the red solid line is the prediction from the general Takahashi-Maekawa model described in the text (with tunneling spin polarization P = 52%). The transparent and tunneling interface limits are shaded in blue and gray, respectively. (b) *RA* dependence of the 5-K ΔR_{NL} compared to the non-local background resistance (R_b). Solid and dashed lines are guides to the eye and the horizontal dashed line at ~2.7 Ω marks the maximum possible ΔR_{NL}, as shown in (a), for these device dimensions and material properties. (c) *RA* dependence (note the wider scale than in (a,b)) of the tunneling spin polarization *P*. Data from NLSVs (including ours) are the red, orange, and yellow points; data from tunneling magnetoresistance (TMR) and superconducting tunneling spectroscopy (STS) are the purple and blue points; the separating vertical dashed line is the 1 kΩμm^2 NLSV limit discussed in the text (and shown in Fig. 3(a)). The colored dashed line is a guide to the eye. The horizontal dashed and dotted lines mark the *P* of Fe and Co, respectively, in the high-*RA* tunneling limit [78–80].

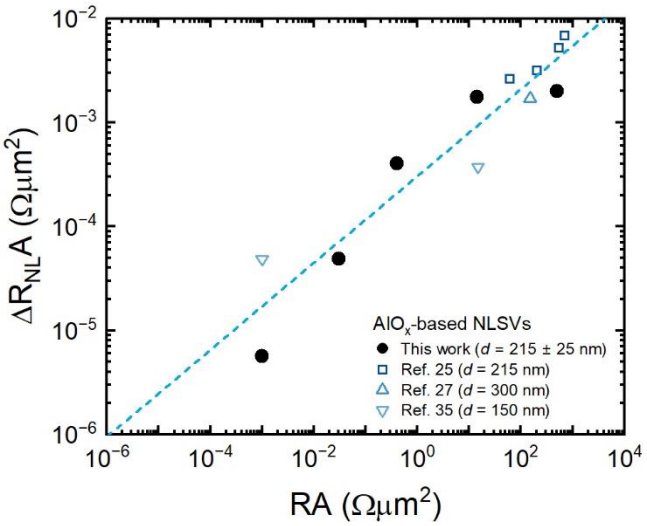

Fig. 7. Non-local resistance change-area product ($\Delta R_{NL}A$) *vs*. the interfacial resistance-area product (RA) for AlO_x-barrier NLSVs in the low-temperature (4-77 K) limit. The data from this work are shown as solid black points, while literature data [25,27,35] are shown as blue open points. The ferromagnet-ferromagnet separation (d) is shown in each case, all values being in the 150-300 nm range. The dashed line is a straight-line fit on this $\log_{10}$-$\log_{10}$ plot with slope ~0.42, *i.e*., a power law with exponent ~0.42.